Supporting Information: Ultra-sharp lateral p-n junctions in modulation-doped graphene

Jesse Balgley,[†] Jackson Butler,[†] Sananda Biswas,[‡] Zhehao Ge,[¶] Samuel Lagasse,[§] Takashi Taniguchi,[‖] Kenji Watanabe,[⊥] Matthew Cothrine,[#] David G. Mandrus,[#] Jairo Velasco Jr.,[¶] Roser Valentí,[‡] and Erik A. Henriksen[*,†]

†*Department of Physics, Washington University in St. Louis, 1 Brookings Dr., St. Louis MO 63130, USA*

‡*Institut für Theoretische Physik, Goethe-Universität Frankfurt, 60438 Frankfurt am Main, Germany*

¶*Physics Department, UC Santa Cruz, 1156 High Street, Santa Cruz, CA 95064, USA*

§*Electronics Science and Technology Division, United States Naval Research Laboratory, Washington, DC 20375, United States*

‖*International Center for Materials Nanoarchitectonics, National Institute for Materials Science, 1-1 Namiki, Tsukuba, 305-0044, Japan*

⊥*Research Center for Functional Materials, National Institute for Materials Science, 1-1 Namiki, Tsukuba, 305-0044, Japan*

#*Material Science & Technology Division, Oak Ridge National Laboratory, Oak Ridge, Tennessee 37831, USA*

@*Department of Material Science and Engineering, University of Tennessee, Knoxville, Tennessee 37996, USA*

E-mail: henriksen@wustl.edu

May 31, 2022

We include additional information relevant to or referenced from the main text, with sections on:

Sample preparation and device fabrication

Device mobilities and mean free paths

Identification of α-$RuCl_3$ crystallographic edges

Analysis of junction resistance data

Scanning tunneling measurements

Density functional theory calculations

Screening of back gate by α-$RuCl_3$

Sample preparation and device fabrication

Graphene, hexagonal boron nitride (hBN), and α-$RuCl_3$ flakes were isolated via mechanical exfoliation. Atomic force microscopy was used to confirm the thickness of the flakes used in each device. Devices D1, D2, D3, and D4 were fabricated using a dry van der Waals stacking technique to pick up and stack layers of graphene, hBN, and α-$RuCl_3$ using an adhesive layer of polypropylene carbonate (PPC) in D1 and poly(bisphenol a) carbonate (PC) in D2, D3, and D4.[1] The aluminum oxide layer in D1 was grown by electron beam evaporation of 1.5 nm of aluminum that was subsequently oxidized. The top gates and contacts used were patterned by electron beam lithography in D1 and photolithography in D2. Contacts and top gates were metallized by thermal evaporation of Cr/Au leads. Devices were etched using XeF2 gas at a chamber pressure of 1500 mTorr for 15 s.[2]

Device mobilities and mean free paths

Electronic transport, including Hall data, in devices D1 and D2 were taken at 4 K in a variable-temperature cryostat using standard low-frequency measurement techniques. Figures S1**a**, **b**, and **c** show the conductivity, mobility, and mean free path, respectively, of device

D1 (AlO_x-spaced) as a function of carrier density for both the g and mod sides. Figure S2**a** shows an image of device D2, which consists of a 5.4-nm-thick flake of α-$RuCl_3$ covered with a 2-nm-thick flake of hBN, topped by a graphene Hall bar that lies partly above the α-$RuCl_3$ and partly on the hBN spacer layer. The Hall bar is capped by a flake of hBN ($\approx$49 nm) supporting a global Cr/Au top gate, and is contacted by Cr/Au leads. The entire device rests on 300 nm of SiO_2 on p-Si; the latter also serves as a global back gate. The stacking order is schematically depicted in Fig. S2**b**. Figure S2**c** shows the mod-side conductivity as a function of density, while Fig. S2**d** shows the mod-side mobility (orange, left axis) and mean free path (black, right axis).

Identification of α-$RuCl_3$ crystallographic edges

Figure S3 shows optical microscope images taken at 50$\times$ magnification of the α-$RuCl_3$ flakes used for modulation doping in device D1 (**a** and **b**) and D2 (**c** and **d**). Figs. S3**a** and **c** have semi-transparent images of the their respective devices overlaid to highlight the device edge used to define the interface between intrinsic and modulation-doped regions. In device D1, the α-$RuCl_3$ edge used to define the junction (indicated by the vertical dashed line in Fig. S3**b** does not appear to be a perfect crystalline edge upon optical inspection. However, the α-$RuCl_3$ edge used to define the junction in D2 (indicated by the vertical dashed line in Fig. S3**d**) appears straight and is oriented nearly 120° from another α-$RuCl_3$ edge, implying that this edge tore along a crystallographic axis during exfoliation.

Analysis of junction resistance data

As described in the main text, to determine the junction resistance, $R_{p\text{-}n}$, we first need to find R_{odd}, which is the difference between the bipolar (p-n) and monopolar (either n-n or p-p) resistances measured (i) in the intrinsic graphene region, (ii) in the modulation-doped region, or (iii) across the interface between the two. Figures S4, S5, S6, and S7 show the data and process for determining R_{odd} for devices D1 and D2.

Figure S4 shows the process for obtaining the three R_{odd} curves in comparing transport between the p-n and n-n regimes for device D1. In each of the first three rows, we show the as-measured resistance (left plot), the resistance re-plotted vs the g- and mod-side carrier densities (center plot), and two line cuts (right plot) taken along the solid (dashed) white lines of the center plot for the same magnitude and sign (same magnitude and opposite sign) of the carrier densities on either side of the interface. The final plot, Fig. S4**j** shows R^{g}_{odd} and R^{mod}_{odd} which contain additional contributions to the resistance due to asymmetry about charge neutrality in the g- and mod-side sheet resistivity, and includes R^{jn}_{odd} which contains a portion of these values, plus the junction resistance $R_{p\text{-}n}$. $R_{p\text{-}n}$ calculated from these curves is shown in the main text Fig. 2**e** as filled circles.

In Fig. S5, we show the companion procedure comparing transport in the p-n and p-p regimes for D1. $R_{p\text{-}n}$ calculated from these curves is shown in the main text Fig. 2**e** as open squares.

In Fig. S6 and S7, the same process is repeated for device D2 except that lost contacts prevented independent measurement of the g-side sheet resistivity. This is irrelevant for Fig. S6, where any g-side Dirac peak asymmetry does not contribute anyway (see main text). Evidently, any g-side asymmetry is negligible in the analysis in Fig. S7, given the close agreement of the two $R_{p\text{-}n}$ curve in Fig. 2**f** of the main text; these would be readily driven apart by any such asymmetry.

As noted in the main text, a dip in R^{jn} leads to an excursion where $R_{p\text{-}n}$ approaches zero in the (p-p)-derived $R_{p\text{-}n}$ trace. While difficult to see in the R^{jn} data (Fig. S8**a**), this feature is obvious in $\partial R^{jn}/\partial n_g$ where it is marked by an arrow in Fig. S8**b**. Its dependence on n_g reveals its origin in the intrinsic graphene side of the device, but it does *not* appear in the sheet resistance measured solely on the g side (Fig. S8**c**), nor does it appear in a derivative w.r.t. n_g (Fig. S8**d**). In other words, it is sampled by the contacts used in measuring R^{jn}, but missed by the geometry of contacts used to measure R^{g}. Meanwhile, our analysis assumes that the g- and mod-side sheet resistances are spatially uniform up to the

interface. However, nonuniformities that may exist close to the interface (such as this) are not necessarily captured in the sheet resistance measurements, and so are not subtracted off when calculating $R_{p\text{-}n}$.

In determining $R_{p\text{-}n}$, we subtracted the asymmetric components of the individual side sheet resistances, R^{g}_{odd} and R^{mod}_{odd}, from the resistance asymmetry measured across the junction, R^{jn}_{odd}. These are shown in Figs. S4**j**, S5**j**, S6**g**, and S7**g**. In the analysis presented in the main text, we multiplied R^{g}_{odd} and R^{mod}_{odd} by geometric scaling factors c_i, where $i = \{g, mod\}$, proportional to the area of each contained between contacts used in measuring R^{jn}. The analysis is robust to variations in c_i up to 20%, easily accommodating small errors in measurement of the device geometry.

In the theory of transport through p-n junction in disordered graphene,[3] transport across the junction is a sum of ballistic and diffusive contributions; which term is dominant depends on the ratio of the carrier density gradient across the interface to the impurity density, $\beta = n'/n^{3/2}_{imp}$, where n_{imp} is determined from the carrier mobility μ by $n_{imp} = e/(h\mu)$. For $\beta \gg 1$ ($\ll 1$) the junction transport is predominantly ballistic (diffusive). To calculate β in these devices, we estimate the density gradient for balanced junctions as $n' = 2|n|/d$, where n is the density of electrons or holes on both sides of the interface. We plot the resulting values of β for devices D1 and D1 as a function of junction width in Fig. S9. Using the experimentally measured mobilities to find n_{imp}, we find both devices easily satisfy $\beta \gg 1$ for any value of d below 300 nm. Accordingly, we compare the experimentally-determined junction resistance $R_{p\text{-}n}$ to the predicted resistance of a ballistic junction, $R_{bal} = c(h/e^2)/(\alpha^{1/6} n'^{1/3} W)$. Here W is the device width, $\alpha \approx 0.3$ (0.5) is the graphene fine structure constant for the device with AlO_x (hBN) spacer, and $c \approx 1$ captures the (α-dependent) effect of many-body effects in the ballistic junction.[4] In this equation the only remaining free parameter is the junction width d in the density gradient n', so d is varied to produce curves of R_{bal} as a function of carrier density that best fit the data. The results are plotted in the main text Fig. 2**e** and **f** as shaded bands that span 100 to 200 nm and 1 to 10 nm, respectively.

Scanning tunneling measurements

Completed devices were annealed in UHV at 400°C for several hours before being transferred into the STM chamber. The STM measurements were conducted in a Createc LT-STM with a vacuum better than 1×10^{-10} mbar at 4.8 K. Electrochemically etched tungsten tips used in the experiments were calibrated by measuring the surface state of Au(111) crystal before all measurements. dI/dV_S spectra were acquired with standard lockin technique by applying a 704 Hz ac modulation to the sample bias, with a setpoint of I=1 nA and a 10 mV excitation. Topographic data was acquired with a setpoint current of I=10-20 pA and a 10 mV ac excitation. The STM topography images were plotted with WSxM.[5]

Density functional theory calculation

Details of calculations DFT structural relaxations of the interface were performed with the projector augmented wave method[6] using the Vienna ab initio simulation package (VASP),[7] using the generalized gradient approximation (GGA) for the exchange-correlation functional. A correction due to van der Waals forces are included through the DFT-D2 scheme of Grimme.[8] The lattice parameter a is chosen in such a way that the graphene layer is not strained (i.e., C-C bond-length remains 1.42 Å after relaxation). A plane-wave cutoff of 600 eV is used for all the geometries with k-point sampling of 1×3×1. For all geometrical optimizations, we have considered Ru atoms to be in ferromagnetic configuration. In order to calculate the amount of charge transfer between the layers, we have used Bader analysis of wavefunctions obtained from VASP calculations.[9] Correlation effects and spin-orbit coupling in this heterostructure system are not expected to affect the value of the charge transfer as observed in the commensurate bilayer case.[10]

To check the effect of orientation of the α-$RuCl_3$ ribbon with respect to the graphene sheet as well as any buckling of graphene, we used four different supercell geometries for structural relaxation: (i) configuration 1, shown in Fig. S10; (ii) configuration 2 which is the same as configuration 1, but with buckled graphene; (iii) configuration 3 where the α-

$RuCl_3$ ribbon is shifted toward the middle of the supercell; and (iv) configuration 4, which is same as configuration 3, with buckled graphene. In the main text we have shown results for configuration 1, found to be the lowest-energy structure. The other configurations are only 14 meV/$RuCl_3$ higher than configuration 1. All these configurations lead to the same values for the charge transfer.

Figure S11 shows the charge density isosurface for a bilayer α-$RuCl_3$ ribbon proximate to graphene. The total charge transfer between graphene and α-$RuCl_3$ is barely changed, with almost all transferred charge residing on the layer nearest the graphene. This can be clearly seen from the values of the charge transfer: in the graphene-facing α-$RuCl_3$ layer, we find -0.0127 electrons/C atom with 0.1020 electrons/$RuCl_3$ unit; and in the second α-$RuCl_3$ layer, just 0.0247 electrons/$RuCl_3$. In comparison, for only a monolayer α-$RuCl_3$ ribbon on graphene these values are -0.01200 electrons/C atom and 0.1200 electrons/$RuCl_3$ unit. Note that these calculations are done in a supercell with slightly smaller lattice parameter ($a =$ 21.34 Å) than otherwise reported in this paper, which may slightly change the quantitative values but not the qualitative result.

Alternative calculation of decay length We calculated the spin-polarized projected density of states onto the C atoms for graphene in contact with α-$RuCl_3$, shown in Fig. S12. From this, we then determined the position-averaged projected DOS, and in Fig. S13 we plot the results at the Fermi level. From these data we determine the decay length in the same spirit as the main text: first we calculate the average of the majority and minority spin channels (the blue line), and then fit this average with the same exponential function as used in the manuscript to find a decay length of 17 Å. This is larger by a factor of two than the decay length for graphene and α-$RuCl_3$ in contact that we obtained from the charge density difference analysis for the same geometry ($\sim$8 Å).

Screening of back gate by α-$RuCl_3$

The carrier densities on the g and mod sides of the devices can be independently tuned due to a surprising ability of α-$RuCl_3$ to screen the electric field sourced from the back gate. This is quite unexpected, since bulk α-$RuCl_3$ is well known to be insulating with a transport gap of $\sim$100s of meV.[11–13] Of course, in the present work the α-$RuCl_3$ has been charge-doped, such that the Fermi energy is calculated to reside just inside the conduction band[10] (presuming there are no impurities or impurity bands). These bands are rather flat and should have a large effective mass; nonetheless it is possible that the α-$RuCl_3$ may become conducting at a level sufficient to screen the back gate electric field. If these samples host impurities sourced from e.g. the ingredients used during growth, the Fermi energy may in fact reside in an impurity band. Regardless of the origin, the fact that α-$RuCl_3$ screens the back gate is well established in three devices discussed in the main text, and enables exploration of p-n junction effects in the graphene.

References

(1) Wang, L.; Meric, I.; Huang, P. Y.; Gao, Q.; Gao, Y.; Tran, H.; Taniguchi, T.; Watanabe, K.; Campos, L. M.; Muller, D. A.; Guo, J.; Kim, P.; Hone, J.; Shepard, K. L.; Dean, C. R. One-Dimensional Electrical Contact to a Two-Dimensional Material. *Science* **2013**, *342*, 614–617.

(2) Son, J.; Kwon, J.; Kim, S.; Lv, Y.; Yu, J.; Lee, J.-Y.; Ryu, H.; Watanabe, K.; Taniguchi, T.; Garrido-Menacho, R.; Mason, N.; Ertekin, E.; Huang, P. Y.; Lee, G.-H.; M. van der Zande, A. Atomically precise graphene etch stops for three dimensional integrated systems from two dimensional material heterostructures. *Nature Communications* **2018**, *9*, 3988.

(3) Fogler, M. M.; Novikov, D. S.; Glazman, L. I.; Shklovskii, B. I. Effect of disorder on a

graphene p-n junction. *Physical Review B* **2008**, *77*, 075420.

(4) Zhang, L.; Fogler, M. Nonlinear Screening and Ballistic Transport in a Graphene *p-n* Junction. *Physical Review Letters* **2008**, *100*, 116804.

(5) Horcas, I.; Fernández, R.; Gómez-Rodríguez, J. M.; Colchero, J.; Gómez-Herrero, J.; Baro, A. M. WSXM: A software for scanning probe microscopy and a tool for nanotechnology. *Review of Scientific Instruments* **2007**, *78*, 013705.

(6) Blöchl, P. E. Projector augmented-wave method. *Physical Review B* **1994**, *50*, 17953–17979.

(7) Kresse, G.; Hafner, J. *Ab initio* molecular dynamics for liquid metals. *Physical Review B* **1993**, *47*, 558–561.

(8) Grimme, S. Semiempirical GGA-type density functional constructed with a long-range dispersion correction. *Journal of Computational Chemistry* **2006**, *27*, 1787–1799.

(9) Henkelman, G.; Arnaldsson, A.; Jónsson, H. A fast and robust algorithm for Bader decomposition of charge density. *Computational Materials Science* **2006**, *36*, 354–360.

(10) Biswas, S.; Li, Y.; Winter, S. M.; Knolle, J.; Valenti, R. Electronic Properties of α-$RuCl_3$ in Proximity to Graphene. *Physical Review Letters* **2019**, *123*, 237201.

(11) Binotto, L.; Pollini, I.; Spinolo, G. Optical and transport properties of the magnetic semiconductor α-$RuCl_3$. *Physica Status Solidi (b)* **1971**, *44*, 245–252.

(12) Mashhadi, S.; Weber, D.; Schoop, L. M.; Schulz, A.; Lotsch, B. V.; Burghard, M.; Kern, K. Electrical Transport Signature of the Magnetic Fluctuation-Structure Relation in α-$RuCl_3$ Nanoflakes. *Nano Letters* **2018**, *18*, 3203–3208.

(13) Zhou, B.; Balgley, J.; Lampen-Kelley, P.; Yan, J.-Q.; Mandrus, D. G.; Henriksen, E. A. Evidence for charge transfer and proximate magnetism in graphene–α-$RuCl_3$ heterostructures. *Physical Review B* **2019**, *100*, 165426.

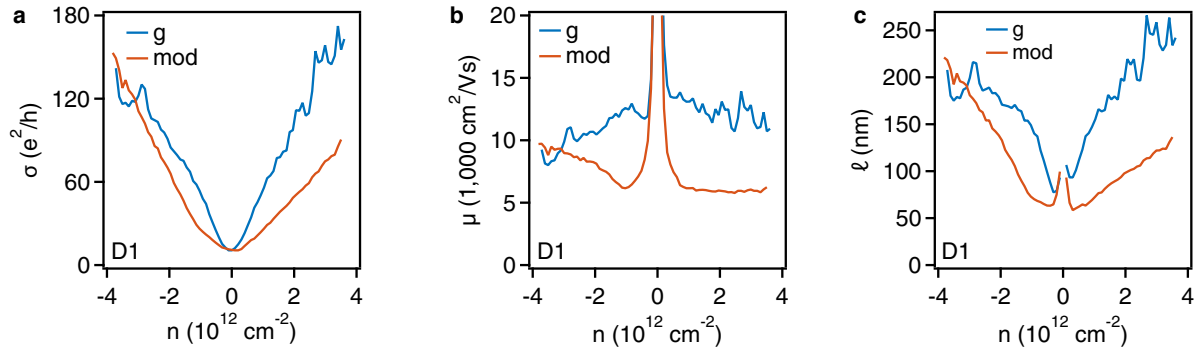


Figure S1: **Electronic transport properties of device D1 (AlO_x spacer).** **a** Conductivities of the g and mod regions of device D1. **b** Mobilities of D1. **c** Mean free paths of D1.

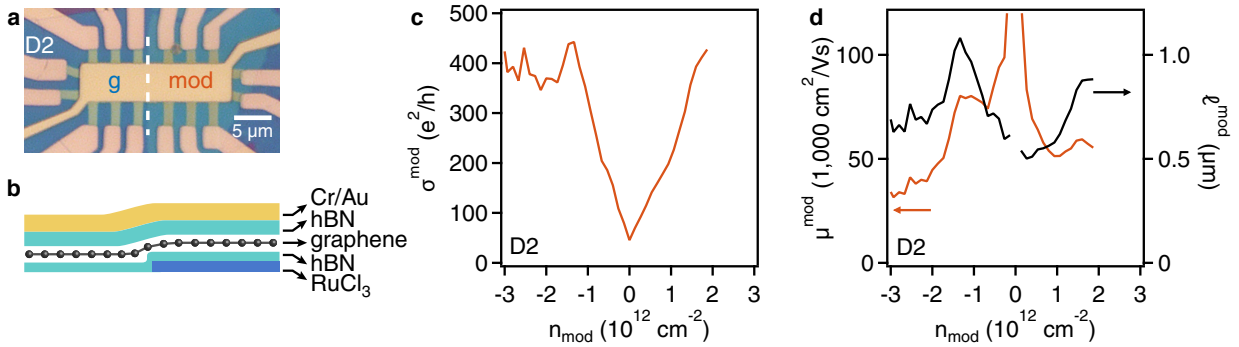


Figure S2: **Electronic transport properties of device D2 (hBN spacer).** **a** Optical micrograph of device D2. **b** Schematic of the stacking arrangement. **c** Conductivity of the mod side of D2. **d** Mobility (orange) and mean free path (black) of D2.

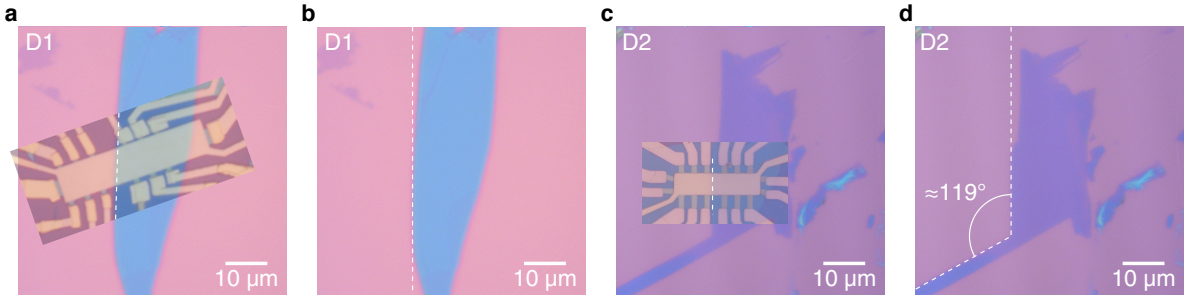


Figure S3: **α-$RuCl_3$ flake edges.** **a** Optical microscope image of the α-$RuCl_3$ flake used in device D1, with the final device image overlaid as a visual aid. **b** The α-$RuCl_3$ flake from **a** with a vertical dashed line indicating the edge used to form the junction interface. **c** Optical microscope image of the α-$RuCl_3$ flake used in device D2, with the final device image overlaid as a visual aid. **d** The α-$RuCl_3$ flake from **c** with a vertical dashed line indicating the edge used to form the junction interface, measured at an angle of ≈119° from another flake edge.

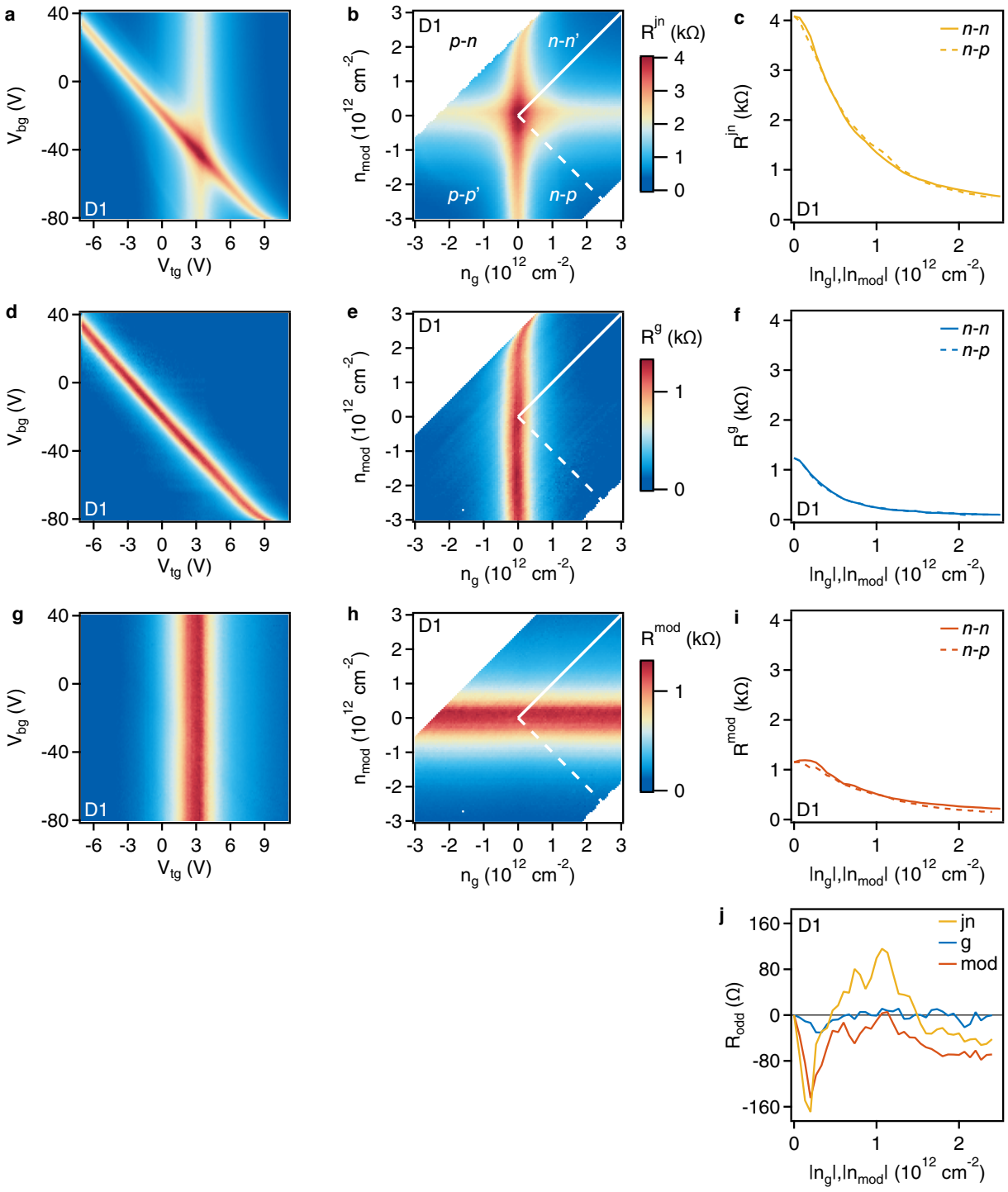


Figure S4: **Comparison of n-n and n-p resistances in device D1.** **a,d,g** Resistance across the junction, and in the g and mod sides as a function of top and bottom gates. **b,e,h** Resistances from **a,d,g** re-plotted as a function of g- and mod-side densities. **c,f,i** Linecuts along solid and dashed lines from **b,e,h**. **j** Differences between the curves in **c,f,i**. Panels **a**, **b**, and **j** are identical to Fig. 2**a**, **b**, and **d** of the main text.

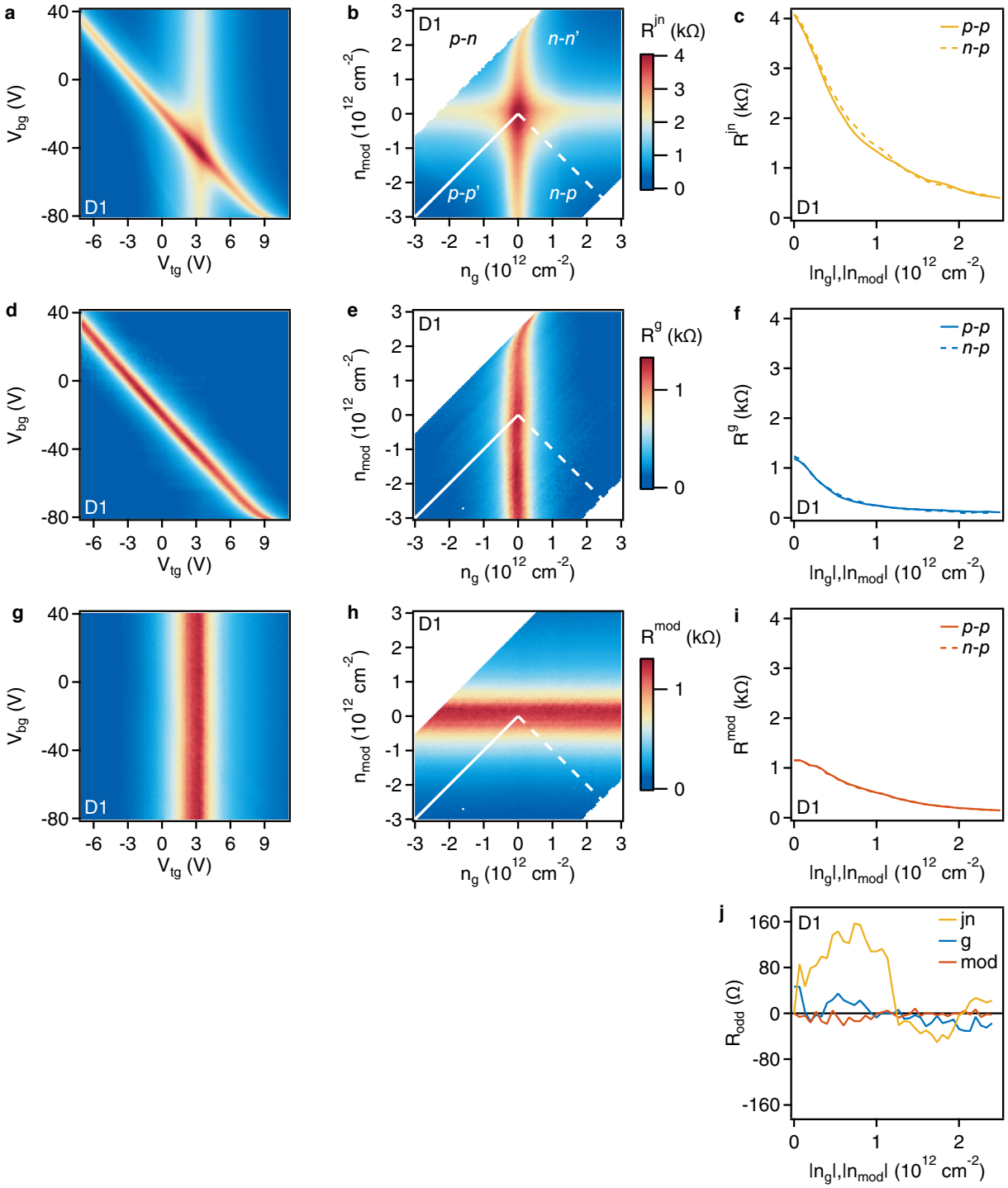


Figure S5: **Comparison of p-p and n-p resistances in device D1.** **a,d,g** Resistance across the junction, and in the g and mod sides as a function of top and bottom gates. **b,e,h** Resistances from **a,d,g** re-plotted as a function of g- and mod-side densities. **c,f,i** Linecuts along solid and dashed lines from **b,e,h**. **j** Differences between the curves in **c,f,i**. Panels **a** and **b** are identical to Fig. 2**a** and **b** of the main text (except for indicating different line cuts).

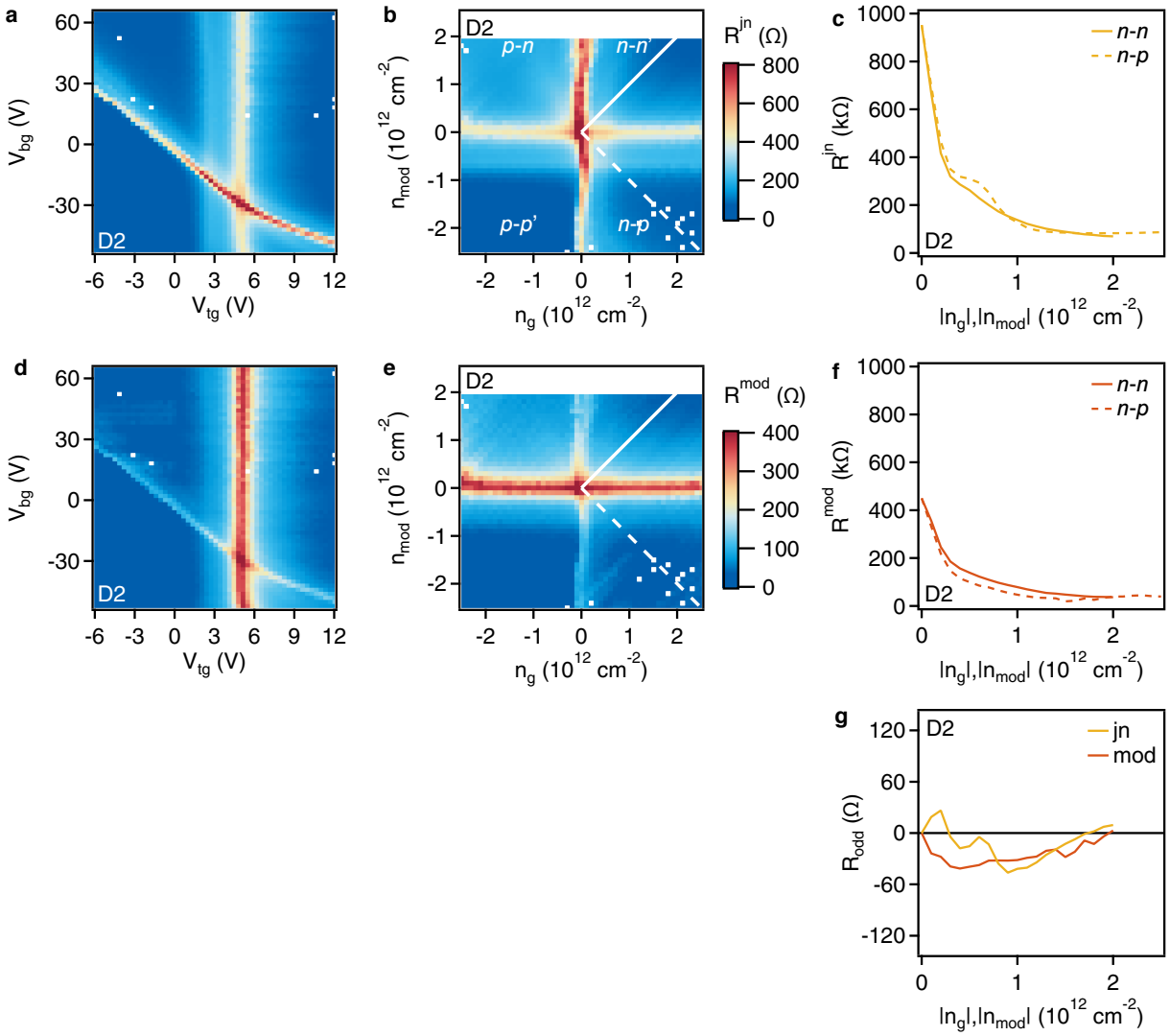


Figure S6: **Comparison of n-n and n-p resistances in device D2. a,d** Resistance across the junction and in the mod side as a function of top and bottom gates. **b,e,h** Resistances from **a,d,g** re-plotted as a function of g- and mod-side densities. **c,f** Linecuts along solid and dashed lines from **b,e**. **j** Differences between the curves in **c,f**.

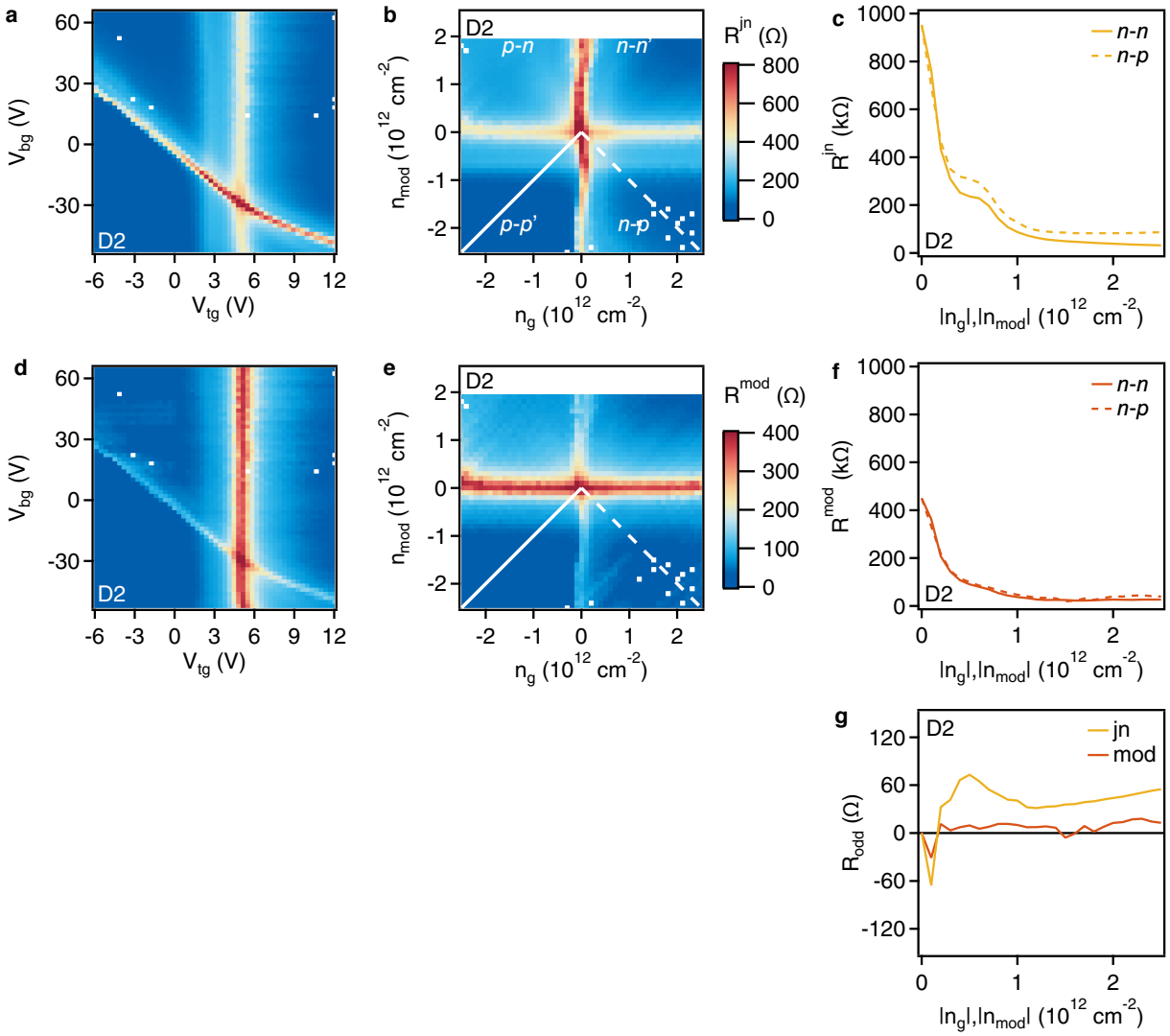


Figure S7: **Comparison of p-p and n-p resistances in device D2. a,d** Resistance across the junction and in the mod side as a function of top and bottom gates. **b,e,h** Resistances from **a,d,g** re-plotted as a function of g- and mod-side densities. **c,f** Linecuts along solid and dashed lines from **b,e**. **j** Differences between the curves in **c,f**.

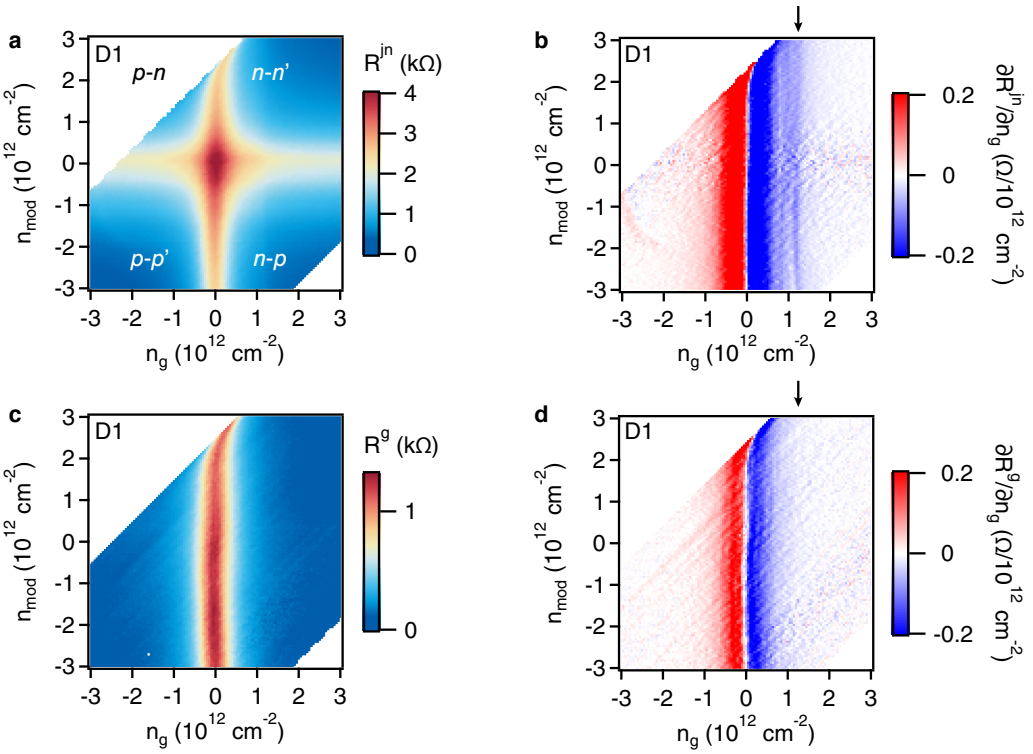


Figure S8: **g-side asymmetry in device D1.** **a** R^{jn} in D1 as a function of g- and mod-side densities. **b** Derivative of **a** taken along the n_g-direction. **c** R^g in D1 as a function of g- and mod- side densities. **d** Derivative of **c** taken along the n_g-direction. Panel **a** is identical to Fig. 2**b** of the main text, except for the lack of line cuts.

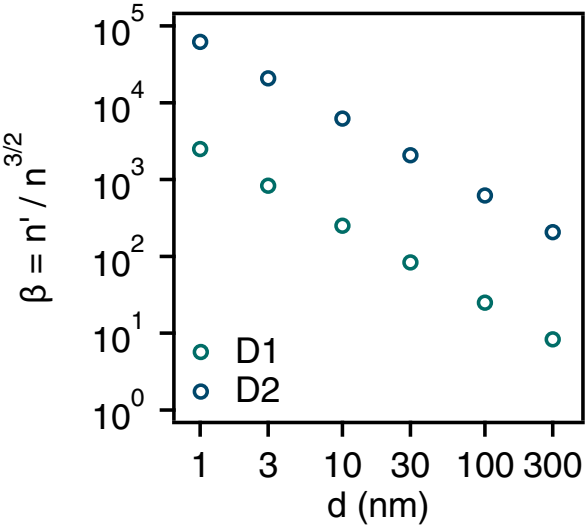


Figure S9: **Calculation of β.** β parameter calculated for n=10^{12} cm^{-2} as a function of junction width d for devices D1 and D2.

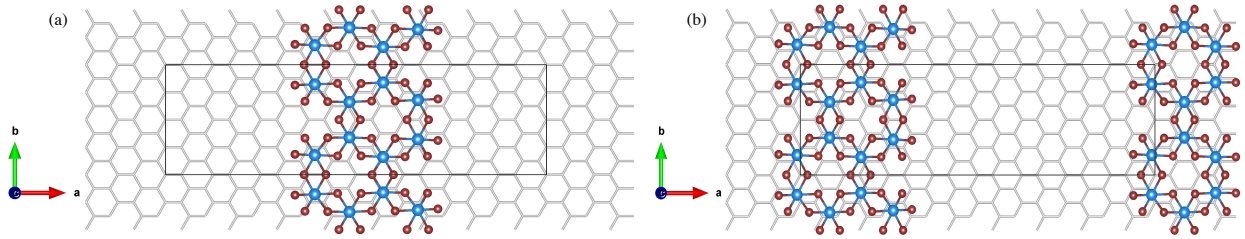


Figure S10: **Configurations considered for DFT calculations.** **a** Configuration 1. **b** Configuration 2. The gray lines indicate the graphene sheet and blue and red spheres represent the Ru and Cl atoms, respectively. The black rectangle shows the supercell in the a-b plane.

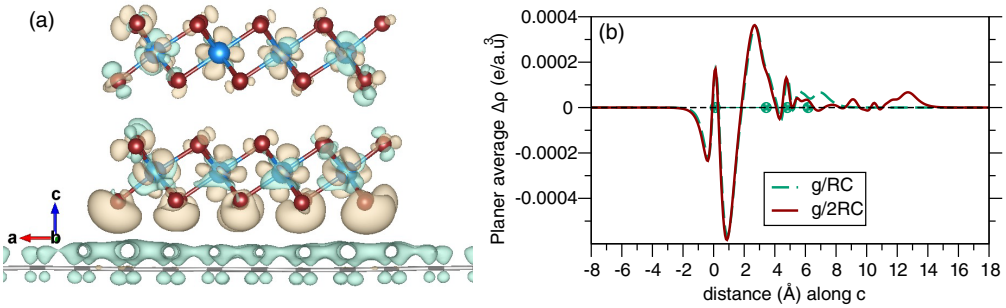


Figure S11: **Charge transfer to a bilayer α-RuCl$_3$ above graphene.** **a** Isosurface plotted at 5×10^{-4} e/a.u.^{3}. **b** Planar average of charge density difference (over $\hat{a}\times\hat{b}$) plotted along $\hat{c}$ direction comparing charge transfer from graphene to both a mono- and bilayer of α-RuCl$_3$.

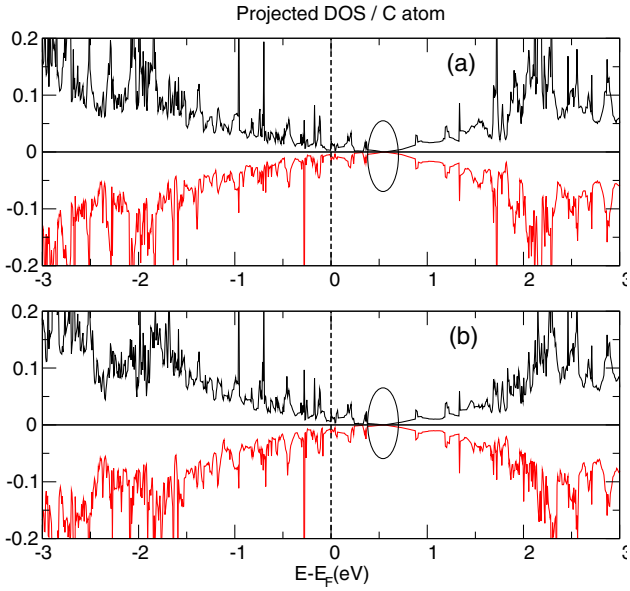


Figure S12: **Spin-polarized projected density of states (PDOS) per C atom.** (a) and (b) represent PDOS on C atoms which are far and near to the edge of α-$RuCl_3$ ribbon, respectively. The black and red colors indicate the spin majority and minority channels, respectively. The Dirac points are circled in both the cases. As we have chosen FM configuration, the α-$RuCl_3$ orbitals and the graphene orbitals overlap over an extended region than reported in Ref.[10]

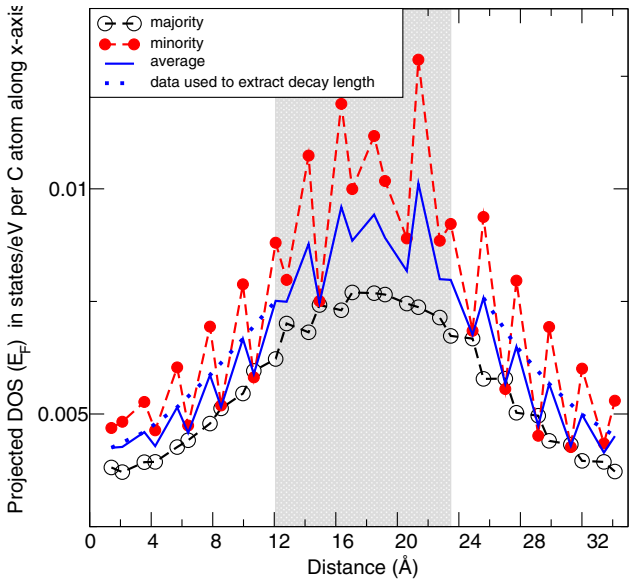


Figure S13: **Spin-polarized projected density of states (PDOS) at the Fermi energy**, per position-averaged C atom along x-direction. The shaded area indicates the position of the α-$RuCl_3$ ribbon.